International Journal of Fracture **49**: 41–67, 1991.

An analysis of dynamic, ductile crack growth in a double edge cracked specimen

A. NEEDLEMAN[1] and V. TVERGAARD[2]
[1]*Division of Engineering, Brown University, Providence, Rhode Island 02912, USA;* [2]*Department of Solid Mechanics, The Technical University of Denmark, Lyngby, Denmark*

Received 15 August 1989; accepted in revised form 12 March 1990

Abstract. Dynamic crack growth is analysed numerically for a plane strain double edge cracked specimen subject to symmetric impulsive tensile loading at the two ends. The material behavior is described in terms of an elastic–viscoplastic constitutive model that accounts for ductile fracture by the nucleation and subsequent growth of voids to coalescence. Two populations of second phase particles are represented, including large inclusions or inclusion colonies with low strength, which result in large voids near the crack tip at an early stage, and small second phase particles, which require large strains before cavities nucleate. The crack growth velocities determined here are entirely based on the ductile failure predictions of the material model, and thus the present study is free from *ad hoc* assumptions regarding appropriate dynamic crack growth criteria. Adiabatic heating due to plastic dissipation and the resulting thermal softening are accounted for in the analyses. Different prescribed impact velocities, inclusion spacings and values of the inclusion nucleation stress are considered. Predictions for the dynamic crack growth behavior and for the time variation of crack tip characterizing parameters are obtained for each case analyzed.

1. Introduction

Investigations of rapid crack growth have mainly focussed on determining critical values of crack tip characterizing parameters such as the energy release rate, the stress intensity factor, or the crack-tip-opening displacement. Once a measure of the frature toughness is known as a function of crack speed, this relationship can be used in computations to predict crack growth.

For a crack travelling at constant speed in an infinite elastic plate Broberg [1] and Freund [2] have obtained exact analytical results for the energy release rate as a function of the crack growth rate, $G(\dot{a})$. The infinite plate problem is special in that stress waves reflected from the boundary are absent. In the more general case, where a structural component or a test specimen is analyzed, stress waves are reflected from the boundaries and may have a strong effect on the crack growth behavior. In such cases the dynamic stress-intensity factor as a function of the crack growth rate, $K_{Id}(\dot{a})$, has often been used as a crack propagation criterion, e.g., by Brickstad and Nilsson [3] who analyzed crack growth and arrest processes in prestressed sheets of hardened carbon steel.

Experimental investigations are necessary to obtain the fracture toughness versus crack speed relationships for different materials. Kalthoff [4] has recently reviewed such experimental work, with the main focus on the shadow optical method of caustics, which can be used on transparent specimens as well as non-transparent specimens (by reflection of light from the surface). In this method the size of the shadow pattern is a measure of the stress intensity factor, and the development of this pattern is followed by a high speed camera.

Kalthoff [4] emphasizes the need to account for dynamic effects in procedures used to evaluate the dynamic fracture toughness, e.g., by applying the concept of impact response curves.

Elastic-plastic finite element analyses of rapid crack propagation have been carried out by Ahmad et al. [5] for a number of cases, using either the crack-tip-opening displacement, the crack-tip-opening angle, the dynamic stress-intensity factor, or a conservation integral to characterize crack advance. These authors find that even for a high-strength steel the effect of crack tip plasticity is significant, so that a conventional elastodynamic analysis is not sufficient. In a viscoplastic finite element analysis of dynamic crack growth carried out by Hoff et al. [6] good qualitative agreement with experiments has been obtained by using crack-tip-opening displacement versus crack advance results for slow growth in the initial part, and subsequently using a fixed critical value of the crack-tip-opening angle as the fracture criterion.

A simple strip yield model has recently been used by Freund and Lee [7] to gain insight in the effect of material rate-dependence on fracture mode transition. Here, the crack advances at constant speed in an infinite elastic solid, with inelastic material behavior represented by a rate-dependent cohesive stress in the yield zone. A critical value of the crack-tip-opening displacement is used as a ductile mode crack growth criterion, while a critical stress at a fixed distance ahead of the crack tip is used as a criterion for cleavage crack growth. Solutions to this problem make it possible to construct curves of critical stress intensity factor versus crack speed for different levels of viscosity, showing the transition between the two different fracture modes.

In the present paper an elastic-viscoplastic model of a ductile porous solid is used in a numerical analysis of dynamic crack growth. Thus, instead of specifying a fracture criterion in terms of a selected crack tip characterizing parameter, the speed of crack growth is directly determined by the micromechanisms of failure incorporated in the material model. Voids nucleate and grow near the crack tip, where high levels of stress and strain occur, and the crack advances when failure by void coalescence is predicted. Ductile porous material models have been used in quasi-static crack analyses by Aoki et al. [8] and Aravas and McMeeking [9] to predict the onset of crack growth, and Needleman and Tvergaard [10] and Becker et al. [11] have carried such analyses further to consider stable crack growth. An extended version of the elastic-viscoplastic porous ductile material model has also been used by Tvergaard and Needleman [12, 13] to analyze the transition between fibrous fracture and cleavage fracture in Charpy V-notch specimens.

A plane strain double edge cracked specimen under dynamic axial loading is considered and adiabatic heating due to plastic deformation is taken into account. It is assumed that the main effects of a temperature increase are changes of the yield strength and thermal expansion. Attention is focussed on circumstances where ductile void growth is the sole micromechanism of failure.

2. Problem formulation

The analysis is based on a convected coordinate Lagrangian formulation of the field equations with the initial unstressed state taken as reference. All field quantities are considered to be functions of convected coordinates, y^i, which serve as particle labels, and time

t. The position, relative to a fixed Cartesian frame, of a material point in the initial configuration is denoted by $\mathbf{x}$. In the current configuration the material point initially at $\mathbf{x}$ is at $\bar{\mathbf{x}}$. The displacement vector $\mathbf{u}$ and the deformation gradient $\mathbf{F}$ are defined by

$$\mathbf{u} = \bar{\mathbf{x}} - \mathbf{x}, \quad \mathbf{F} = \frac{\partial \bar{\mathbf{x}}}{\partial \mathbf{x}}. \tag{2.1}$$

Base vectors in the reference configuration (unbarred) and in the current configuration (barred) are given by

$$\mathbf{g}_i = \frac{\partial \mathbf{x}}{\partial y^i}, \quad \bar{\mathbf{g}}_i = \frac{\partial \bar{\mathbf{x}}}{\partial y^i}, \tag{2.2}$$

$$\mathbf{g}^i = g^{ij}\mathbf{g}_j, \quad \bar{\mathbf{g}}^i = \bar{g}^{ij}\bar{\mathbf{g}}_j, \tag{2.3}$$

where g^{ij} and $\bar{g}^{ij}$ are, respectively, the inverses of the metric tensors $g_{ij} = \mathbf{g}_i \cdot \mathbf{g}_j$ and $\bar{g}_{ij} = \bar{\mathbf{g}}_i \cdot \bar{\mathbf{g}}_j$.

The dynamic principle of virtual work is written as

$$\int_V \tau^{ij}\delta E_{ij}\,\mathrm{d}V = \int_S T^i \delta u_i\,\mathrm{d}S - \int_V \rho \frac{\partial^2 u^i}{\partial t^2}\delta u_i\,\mathrm{d}V, \tag{2.4}$$

where V, S and ρ are the volume, surface and mass density, respectively, of the body in the reference configuration.

Here, τ^{ij} are the contravariant components of Kirchoff stress on the deformed convected coordinate net, $\boldsymbol{\tau} = J\boldsymbol{\sigma}$, with $\boldsymbol{\sigma}$ the Cauchy stress and $J = \det(\mathbf{F})$. Also,

$$T^i = (\tau^{ij} + \tau^{kj}u^i_{\ k})v_j, \tag{2.5}$$

$$E_{ij} = \tfrac{1}{2}(u_{i,j} + u_{j,i} + u^k_{\ ,i}u_{k,j}), \tag{2.6}$$

where $\mathbf{v}$ is the surface normal in the reference configuration, u_j are the components of the displacement vector on base vectors in the reference configuration, and $(\ )_{,j}$ denotes covariant differentiation in the reference frame.

The computations are carried out for a double edge cracked rectangular bar as shown in Fig. 1. Plane strain conditions are assumed to prevail and a Cartesian coordinate system is used as reference, with the y^1–y^2-plane being the plane of deformation. The specimen dimensions are taken as $w = 100\,\mathrm{mm}$ and $b = 200\,\mathrm{mm}$, with an initial crack length $a = 17.5\,\mathrm{mm}$. Symmetry about both the y^1 and y^2 axes is assumed. The boundary conditions on the quadrant analyzed numerically are

$$T^1 = 0, \quad T^2 = 0 \quad \text{on } y^1 = -w, \tag{2.7}$$

$$u^1 = 0, \quad T^2 = 0 \quad \text{on } y^1 = 0, \tag{2.8}$$

$$T^1 = 0, \quad T^2 = 0 \quad \text{on } y^2 = 0 \text{ and } y^1 < -(w - a), \tag{2.9a}$$

$$u_2 = 0, \quad T^1 = 0 \quad \text{on } y^2 = 0 \text{ and } y^1 > -(w - a), \tag{2.9b}$$

$$u_2 = U(t), \quad T^1 = 0 \quad \text{on } y^2 = b. \tag{2.10}$$

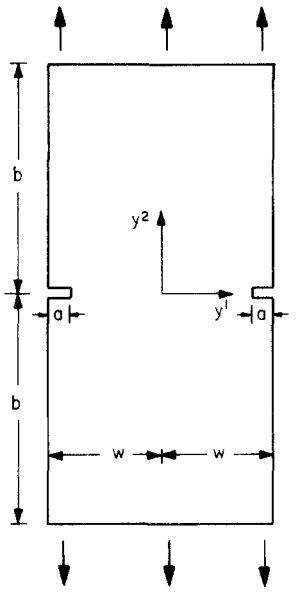

Fig. 1. Geometry of the double edge cracked specimen.

The function $U(t)$ in (2.7) is taken as

$$U(t) = \begin{cases} V_1 t^2/(2t_1), & \text{for } t \leqslant t_1; \\ V_1(t - t_1/2), & \text{for } t > t_1, \end{cases} \tag{2.11}$$

with V_1 being a prescribed velocity and t_1 the rise time.

The basis for the constitutive model is a flow potential, introduced by Gurson [14, 15], that characterizes the porosity in terms of a single scalar internal variable, f, the void volume fraction

$$\Phi = \frac{\sigma_e^2}{\bar{\sigma}^2} + 2q_1 f^* \cosh\left(\frac{3q_2\sigma_h}{2\bar{\sigma}}\right) - 1 - q_1^2 f^{*2} = 0. \tag{2.12}$$

Here, $\bar{\sigma}$ is the average strength of the matrix material and

$$\sigma_e^2 = \tfrac{3}{2}\boldsymbol{\sigma}' : \boldsymbol{\sigma}' \quad \sigma_h = \tfrac{1}{3}\boldsymbol{\sigma} : \mathbf{I} \quad \boldsymbol{\sigma}' = \boldsymbol{\sigma} - \sigma_h \mathbf{I}. \tag{2.13}$$

In the rate-independent constitutive relations proposed by Gurson [14, 15] Φ serves as a yield function. In the viscoplastic formulation, Pan et al. [16], there is no yield condition and Φ is a plastic potential.

The parameters q_1 and q_2 were introduced by Tvergaard [17, 18] to bring predictions of the model into closer agreement with full numerical analyses of a periodic array of voids. The function f^* was proposed by Tvergaard and Needleman [19] to account for the effects of rapid void coalescence at failure. Initially $f^* = f$ as originally proposed by Gurson [14, 15], but at some critical void fraction, f_c the dependence of f^* on f is changed. The function is

expressed by,

$$f^* = \begin{cases} f & f \leqslant f_c; \\ f_c + \dfrac{f_u^* - f_c}{f_f - f_c}(f - f_c) & f \geqslant f_c. \end{cases} \tag{2.14}$$

The constant f_u^* is the value of f^* at zero stress in (2.9), i.e., $f_u^* = 1/q_1$. As $f \to f_f, f^* \to f_u^*$ and the material loses all stress carrying capacity.

In general the evolution of the void volume fraction results from growth of existing voids and nucleation of new voids,

$$\dot{f} = \dot{f}_{\text{growth}} + \dot{f}_{\text{nucleation}}. \tag{2.15}$$

The rate of increase of void volume fraction due to the growth of existing voids is determined from the condition that the matrix material is plastically incompressible,

$$\dot{f}_{\text{growth}} = (1 - f)\mathbf{d}^p : \mathbf{I}. \tag{2.16}$$

The contribution resulting from the nucleation of new voids is taken to be given by,

$$\dot{f}_{\text{nucleation}} = \mathscr{D}\dot{\bar{\varepsilon}} + \mathscr{B}(\dot{\sigma}_e + \dot{\sigma}_h). \tag{2.17}$$

As suggested by Chu and Needleman [20], void nucleation is taken to follow a normal distribution. For plastic strain controlled nucleation,

$$\mathscr{D} = \frac{f_N}{s_N\sqrt{2\pi}} \exp\left[-\frac{1}{2}\left(\frac{\bar{\varepsilon} - \varepsilon_N}{s_N}\right)^2\right] \quad \mathscr{B} = 0, \tag{2.18}$$

while for stress controlled nucleation

$$\mathscr{B} = \frac{f_N}{s_N\sqrt{2\pi}} \exp\left[-\frac{1}{2}\left(\frac{(\bar{\sigma} + \sigma_h) - \sigma_N}{s_N}\right)^2\right] \quad \mathscr{D} = 0. \tag{2.19}$$

The plastic part of the rate of deformation, $\mathbf{d}^p$ is taken in a direction normal to the flow potential,

$$\mathbf{d}^p = \dot{\Lambda}\frac{\partial \Phi}{\partial \boldsymbol{\sigma}}. \tag{2.20}$$

By setting the plastic work rate equal to the matrix dissipation,

$$\boldsymbol{\sigma} : \mathbf{d}^p = (1 - f)\bar{\sigma}\dot{\bar{\varepsilon}} \tag{2.21}$$

the plastic flow proportionality factor, $\dot{\Lambda}$ is determined to be,

$$\dot{\Lambda} = \frac{(1 - f)\bar{\sigma}\dot{\bar{\varepsilon}}}{\boldsymbol{\sigma} : \dfrac{\partial \Phi}{\partial \boldsymbol{\sigma}}}. \tag{2.22}$$

The matrix material is characterized as a thermally softening viscoplastic solid. The matrix plastic strain rate, $\dot{\bar{\varepsilon}}$, is given by

$$\dot{\bar{\varepsilon}} = \dot{\varepsilon}_0 \left(\frac{\bar{\sigma}}{g(\bar{\varepsilon}, T)} \right)^{1/m}. \tag{2.23}$$

Here, T is the temperature and

$$g(\bar{\varepsilon}, T) = \sigma_0[1 - \beta(T - T_0)][1 + \bar{\varepsilon}/\varepsilon_0]^N. \tag{2.24}$$

The heating due to plastic dissipation is accounted for and adiabatic conditions are assumed so that balance of energy gives

$$\rho c_p \frac{\partial T}{\partial t} = \chi \boldsymbol{\tau} : \mathbf{d}^p, \tag{2.25}$$

where ρ is the density in the reference configuration, c_p is the heat capacity, and the parameter χ specifies the fraction of plastic stress working converted to heat; χ is taken to have the value 0.90, which is a typical value for metals, Taylor and Quinney [21].

The rate of deformation is as the sum of an elastic part, a plastic part and a part due to thermal straining. Hence,

$$\mathbf{d} = \mathbf{d}^e + \mathbf{d}^p + \mathbf{d}^T, \tag{2.26}$$

with $\mathbf{d}^p$ as given by (2.20), with the elasticity approximated by the hypoelastic relation

$$\mathbf{d}^e = \mathscr{L}^{-1} : \hat{\boldsymbol{\sigma}} \tag{2.27}$$

and with

$$\mathbf{d}^T = \alpha \dot{T} \mathbf{I}, \tag{2.28}$$

where $\hat{\boldsymbol{\sigma}}$ is the Jaumann stress rate, $\mathscr{L}$ is the tensor of elastic moduli and α is the thermal expansion coefficient. Substituting into (2.26) and inverting gives

$$\hat{\boldsymbol{\sigma}} = \mathscr{L} : \mathbf{d} - \dot{\Lambda} \mathscr{L} : \frac{\partial \Phi}{\partial \boldsymbol{\sigma}} - \alpha \dot{T} \mathscr{L} : \mathbf{I}. \tag{2.29}$$

On the current convected coordinates

$$\mathscr{L}^{ijkl} = \frac{E}{1 + \nu} \left[\tfrac{1}{2}(\bar{g}^{ik}\bar{g}^{jl} + \bar{g}^{jk}\bar{g}^{il}) + \frac{\nu}{1 - 2\nu} \bar{g}^{ij}\bar{g}^{kl} \right]. \tag{2.30}$$

In the calculations here, the material parameters are specified to have values representative of structural steels; $E = 211\,\text{GPa}$, $\nu = 0.3$, $\sigma_0 = 1000\,\text{MPa}$, $N = 0.1$ and $m = 0.01$. The reference temperature T_0 is taken as 20°C, $\beta = 0.0016$ per °C, $c_p = 465\,\text{J/(kg °C)}$ and $\alpha = 1 \times 10^{-5}$ per °C.

For the viscoplastic material, wave speeds are determined by the elastic moduli. With $\rho = 7800\,\mathrm{kg\,m^{-3}} = 7.8 \times 10^{-3}\,\mathrm{MPa/(m\,s^{-1})^2}$, the speeds of the elastic distortion and dilatation waves are

$$c_0 = \sqrt{\frac{G}{\rho}} = 3.23 \times 10^3\,\mathrm{m\,s^{-1}} \quad c_1 = \sqrt{\frac{2G(1-\nu)/(1-2\nu)}{\rho}} = 6.03 \times 10^3\,\mathrm{m\,s^{-1}}, \tag{2.31}$$

where $2G = E/(1+\nu)$.

For a plane strain crack, growing along the y^1-axis, the energy released per unit crack advance is, Nakamura et al. [22],

$$\mathscr{G} = \lim_{\Gamma \to 0} \int_\Gamma [(W + L)\,\mathrm{d}y^2 - T^i u_{i,1}\,\mathrm{d}s], \tag{2.32}$$

where Γ is a path in the reference configuration surrounding the defect tip and W and L are the stress-work and kinetic energy density, respectively, with [23]

$$W = \int_0^{E_{ij}} \tau^{ij}\,\mathrm{d}E_{ij} - \alpha \int_0^T \tau_k^k\,\mathrm{d}T \quad L = \tfrac{1}{2}\rho \frac{\partial u^i}{\partial t}\frac{\partial u_i}{\partial t}. \tag{2.33}$$

Using the general procedure for treating crack tip contour integrals, Moran and Shih [24, 25], $\mathscr{G}$ can be expressed as

$$\mathscr{G} = J = \int_\Gamma [(W + L)\,\mathrm{d}y^2 - T^i u_{i,1}\,\mathrm{d}s] + \int_A \left[\alpha\tau_k^k T_{,1} + \rho\frac{\partial^2 u^i}{\partial t^2} u_{i,1} - \rho\frac{\partial u^i}{\partial t}\left(\frac{\partial u_i}{\partial t}\right)_{,1}\right] \mathrm{d}A, \tag{2.34}$$

where A is the area inside the contour Γ. In obtaining (2.34), the relation $W_{,1} = \tau^{ij}E_{ij,1} - \alpha\tau_k^k T_{,1}$ has been used.

The expression (2.34) gives the generalization of Rice's [30] J integral for dynamic loading conditions. The main significance of J for stationary cracks under quasi-static loading conditions stems from its role as a characterizing parameter for near tip field quantities, even for a path dependent Mises flow theory solid. In the circumstances analysed here, J in (2.34) does not necessarily serve as such a characterizing parameter.

3. Solution procedure

The transient analysis for the double edge cracked specimen is carried out using a finite element approximation for the displacement components in the dynamic principle of virtual work (2.4). Due to symmetries of the specimen and the assumed symmetry of loading, as specified by (2.7) to (2.11), only one quarter of the specimen needs to be analyzed numerically. The mesh used for the computations is shown in Fig. 2, where each quadrilateral is built up of four triangular, linear displacement elements. In front of the crack tip a uniform mesh is used in a small rectangular region to describe crack growth, Fig. 2b. The length of this region in the direction of crack advance is chosen as $0.015w$ (1.5 mm) and the height is $0.7 \times 10^{-3}w$ (0.07 mm). The quadrilateral elements in the uniform region are rectangles of dimension 0.0214 mm × 0.0175 mm.

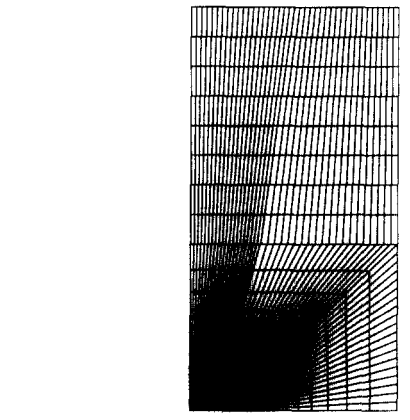

(a)

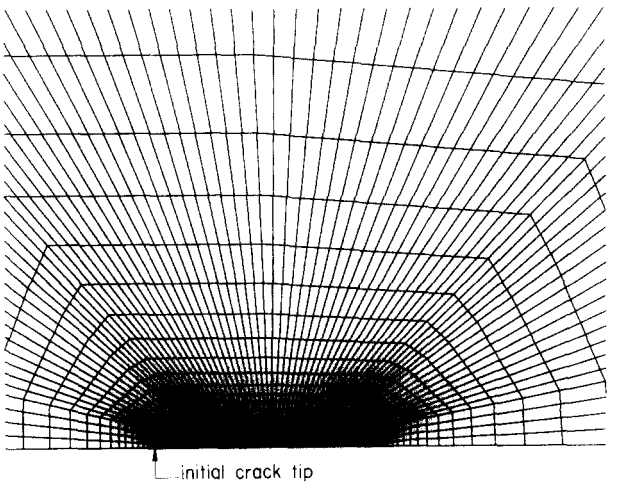

(b)

Fig. 2. Finite element mesh. Each quadrilateral consists of four "crossed" triangles. (a) Quadrant analyzed numerically. (b) Inner mesh showing the location of the initial crack tip. In presenting the numerical results, attention will focus on distributions of field quantities in this region.

The crack growth mechanism analyzed here involves two populations of void nucleating particles; large particles that nucleate voids at relatively small strains and smaller particles that nucleate voids at much larger strains, see also Needleman and Tvergaard [10]. The small scale particles are taken to be uniformly distributed and nucleate by a plastic strain controlled mechanism (2.18). The large particles are modelled as "islands" of the amplitude of the void nucleation function (2.19) corresponding to stress controlled nucleation. Thus, in the present plane strain analysis the large particles are cylindrical in shape, and the spatial distribution of the amplitude f_N in (2.19), defining an island with radius r_0 and center at (y_0^1, y_0^2) is taken to be of the form

$$f_N = \bar{f}_N \exp\{-[(y^1 - y_0^1)^2 + (y^2 - y_0^2)^2]/r_0^2\}. \tag{3.1}$$

The "islands" of void nucleation amplitude in (3.1) will be referred to as particles or inclusions, although only the void nucleation characteristics of second phase particles or inclusions are modelled. Since the difference in material properties between the particle and the background material is not accounted for, any difference in response between the particle and the background material is a consequence of void nucleation and growth.

The equations resulting from substituting the finite element approximation of $\mathbf{u}$ into (2.4) are of the form

$$\mathbf{M}\frac{\partial^2 \mathbf{U}}{\partial t^2} = \mathbf{F}, \tag{3.2}$$

where $\mathbf{M}$ is a mass matrix, $\mathbf{U}$ is the nodal displacement vector and $\mathbf{F}$ is the nodal force vector. As in a previous transient analysis for the Charpy V-notch test, Tvergaard and Needleman [13], the equations of motion (3.2) are integrated numerically by an explicit integration procedure, the Newmark β-method with $\beta = 0$, Belytschko et al. [26]. A lumped mass matrix is used instead of the consistent mass matrix, since this has been found preferable for explicit time integration procedures, from the point of view of accuracy as well as computational efficiency, Krieg and Key [27]. The boundary conditions (2.11) are expressed in terms of a prescribed $\partial U/\partial t$, which is constant, apart from an initial time interval $[0, t_1]$ where the velocity is ramped up linearly.

In the explicit time integration procedure the maximum stable time step is limited by the criterion $\Delta t \leqslant \min(\Delta l/c)$, where Δl is the minimum element dimension, c is the maximum wave speed (see (2.31)), and the minimization is taken over all elements. Another limitation is due to the elastic-viscoplastic constitutive description. After each time step the values of the stress components, void volume fraction, matrix flow stress, etc., are updated using (2.15) to (2.29). Due to the large exponent $1/m$ in (2.23), small oscillations in $\bar{\sigma}$ may result in violent oscillations of the stresses obtained from (2.29) during updating, unless the time step is sufficiently small. This limitation on Δt can be relaxed somewhat by using the forward gradient method proposed by Peirce et al. [28].

Since heating due to plastic dissipation is accounted for in the present analysis, the forward gradient method has to be modified accordingly. In the constitutive relations the matrix plastic strain rate, $\dot{\bar{\varepsilon}}$, is expressed as a linear interpolation between the rates at time t and $t + \Delta t$, respectively,

$$\dot{\bar{\varepsilon}} = (1 - \theta)\dot{\bar{\varepsilon}}_t + \theta\dot{\bar{\varepsilon}}_{t+\Delta t} \tag{3.3}$$

and a Taylor series expansion is used to estimate the value of the rate at time $t + \Delta t$

$$\dot{\bar{\varepsilon}}_{t+\Delta t} = \dot{\bar{\varepsilon}} + \Delta t\left[\frac{\partial \dot{\bar{\varepsilon}}}{\partial \bar{\sigma}}\dot{\bar{\sigma}} + \frac{\partial \dot{\bar{\varepsilon}}}{\partial \bar{\varepsilon}}\dot{\bar{\varepsilon}} + \frac{\partial \dot{\bar{\varepsilon}}}{\partial T}\dot{T}\right]. \tag{3.4}$$

Here, with the assumption of adiabatic conditions, (2.25) and (2.21) give the following expression for the rate of change of the temperature

$$\dot{T} = \frac{\chi}{\rho c_p}(1 - f)\bar{\sigma}\dot{\bar{\varepsilon}} \tag{3.5}$$

to be substituted into (3.4) and the last term of (2.29). Apart from these two modifications due to the non-zero value of $\dot{T}$, the remaining part of the derivation of the rate dependent tangent modulus expression follows that given by Peirce et al. [28] and is not repeated here.

Material failure by void coalescence is implemented in the numerical computations via the element vanish technique of Tvergaard [29]. When the failure condition is met in an element, the contributions of this element to the virtual work are neglected, and the nodal forces arising from the remaining stresses in a failed element are gradually released in subsequent increments. As in previous analyses, e.g., [10–13], failure of an element is taken to occur slightly before the total loss of stress carrying capacity, when $f^* = 0.9 f_u^*$. In the present investigation the speed of crack growth is directly determined by this occurrence of material failure, leading to vanishing element stiffnesses ahead of the crack tip.

4. Results

Although no attempt is made to model a specific real material, the material parameters have been specified to be representative of high strength steels. The uniformly distributed small particles are taken to represent carbide particles that are typically of the order of 0.1 μm in size, while the larger particles represent inclusions. The size and spatial distribution of the larger void nucleating particles is given by (3.1), with the inclusion size specified by $r_0 = 10 \times 10^{-6}\,\text{m} = 10\,\mu\text{m}$. In the present calculations, attention is confined to inclusions lying along the initial crack line. The initial spacing between inclusion centers is denoted by D, which serves as a characteristic length scale. It is worth noting that fully ductile dynamic crack growth, where the fracture mechanism involves two size scales of voids as modelled here, has been observed in steels by Cho et al. [35].

Inertial effects on void growth are not incorporated into the porous plastic constitutive relation described in Section 2. Hence, inertial effects are ignored for the small carbide particles. However, when failure occurs in the large inclusions discrete voids form and the inertia of the material surrounding these discrete voids is accounted for in the analysis.

Void nucleation in the large inclusions is governed by the stress nucleation criterion (2.19), with $\bar{f}_N = 0.04$ in (3.1) and $s_N = 100\,\text{MPa}$ in (2.19). Void nucleation at the uniformly distributed small particles is strain controlled with amplitude $f_N = 0.02$, $\varepsilon_N = 0.3$ and $s_N = 0.10$ in (2.18). Void growth is described by employing $q_1 = 1.25$ and $q_2 = 1.0$ in (2.12), and $f_c = 0.12$ and $f_f = 0.25$ in (2.14). The values $q_1 = 1.25$ and $q_2 = 1.0$ are chosen based on the analyses in [31, 32] which indicated good agreement between the predictions for void growth and stress-strain response of the Gurson [14, 15] constitutive relation and finite element cell model calculations for this choice of parameter values.

Attention is focussed on four cases: (a) $\sigma_N = 1100\,\text{MPa}$, $D = 100\,\mu\text{m}$, $V_1 = 20\,\text{m/sec}$; (b) $\sigma_N = 1100\,\text{MPa}$, $D = 100\,\mu\text{m}$, $V_1 = 30\,\text{m s}^{-1}$; (c) $\sigma_N = 2200\,\text{MPa}$, $D = 100\,\mu\text{m}$, $V_1 = 20\,\text{m s}^{-1}$; and (d) $\sigma_N = 1100\,\text{MPa}$, $D = 200\,\mu\text{m}$, $V_1 = 20\,\text{m s}^{-1}$. Case (a) serves as a reference case. In case (b) all material properties are identical to those in the reference case, but the imposed velocity is increased. Cases (c) and (d) each differ from the reference case by one characteristic of the large inclusions. For case (c) the nucleation stress is a factor of two larger than in the reference case, but the reference spacing is maintained. For case (d) the particle spacing is twice the reference spacing and the nucleation stress is the same as in the reference case. In the following, cases (b), (c) and (d) will be denoted by the value of the

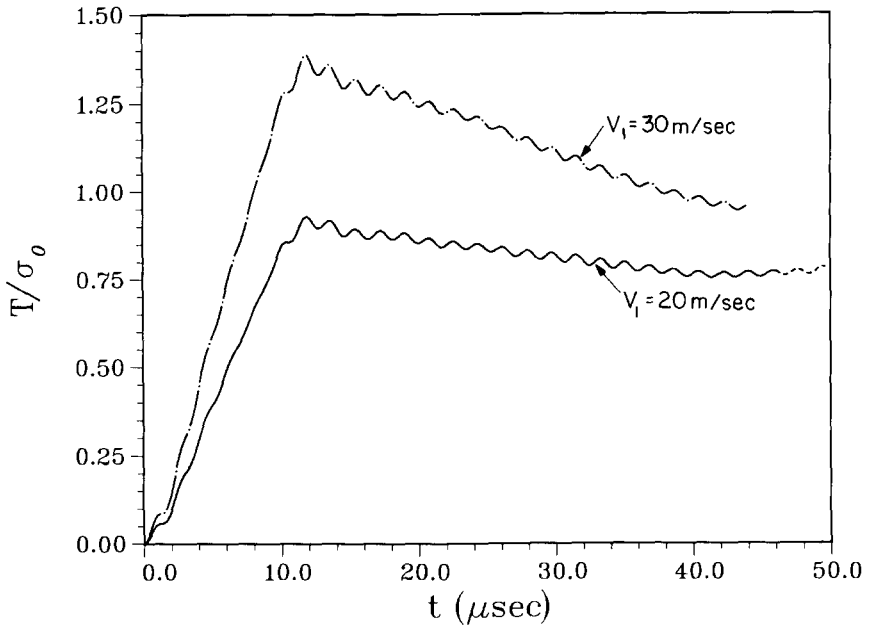

Fig. 3. Traction, force per unit initial area, at the impacted end versus time. The traction is normalized by the reference strength σ_0. In all calculations here $\sigma_0 = 1000\,\text{MPa}$.

parameter that differs from the corresponding reference value. Note that the elastic properties, the strain and strain rate hardening properties, and the parameters characterizing void nucleation, growth and coalescence in the background Gurson material are identical for all four cases.

Figure 3 shows computed curves of traction versus end-displacement. The rise time of $t_1 = 10\,\mu\text{sec}$ in (2.11) is evident in this figure. The oscillations on the traction-displacement curves are a consequence of the discretization. Calculations were also carried out for an uncracked specimen with the material characterized as a rate dependent Mises solid having the same elastic and plastic properties used for the calculations in Fig. 3. The quadrilateral mesh for these calculations consisted of a 20×40 array of identical squares (each composed of four crossed triangles). For both $V_1 = 20\,\text{m}\,\text{s}^{-1}$ and $V_1 = 30\,\text{m}\,\text{s}^{-1}$, the traction-displacement curves computed using the square mesh are the mean curves about which the traction-displacement curves in Fig. 3 oscillate. Crack growth has no effect on the traction-displacement curves in Fig. 3, since the calculations are terminated before there is time for a wave to reflect back from the crack line ($y^2 = 0$) to the impacted end $y^2 = b = 200\,\text{mm}$ (this time is $(2 \times 0.2\,\text{m})/(6030\,\text{m}\,\text{s}^{-1}) \approx 66\,\mu\text{s}$). Hence, the three cases with $V_1 = 20\,\text{m}\,\text{s}^{-1}$ have traction-displacement curves that coincide in Fig. 3.

For the reference case, Fig. 4 shows contours of constant Mises effective stress in the quadrant of the specimen analyzed numerically. In this figure, as in subsequent figures showing stress contours, the stress values are normalized by σ_0. Since in all the calculations here $\sigma_0 = 1000\,\text{MPa}$, the stress contour levels noted on the figure are stress values in units of GPa. Figure 4a shows a stage shortly before the wave has reached the crack line. The stress state prevailing in Fig. 4a is in very good agreement with that obtained from the square 20×40 mesh calculation with $V_1 = 20\,\text{m}\,\text{s}^{-1}$. Figure 4b is before the initiation of crack growth and Fig. 4c is shortly after the onset of crack growth. At $t = 46.25\,\mu\text{s}$, the crack has

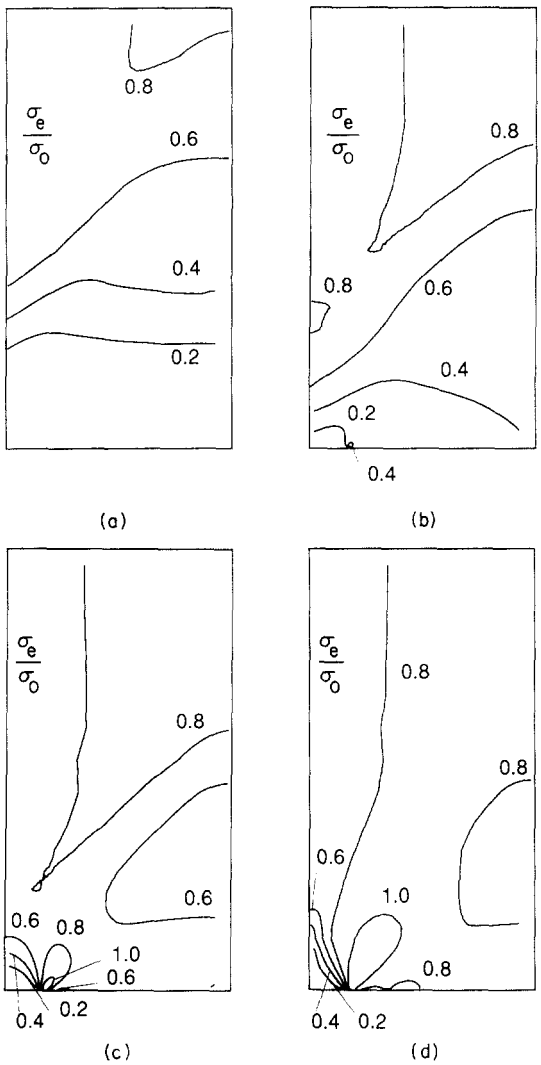

Fig. 4. Contours of constant Mises effective stress, σ_e, for the reference case in the quadrant analyzed numerically. (a) $t = 29.20\,\mu s$ (b) $t = 37.15\,\mu s$ (c) $t = 41.70\,\mu s$ (d) $t = 46.25\,\mu s$, $\sigma_0 = 1000\,MPa$.

grown to near the end of the uniform mesh region in Fig. 2b. With V_1 $20\,m\,s^{-1}$, the specimen remains elastic except for the plastic zone emanating from the crack. With $V_1 = 30\,m\,s^{-1}$ some yielding occurs near the end $y^2 = b$, which results in the traction decrease seen in Fig. 3. Nevertheless, fully plastic conditions are not achieved over the time interval, $t \leqslant 43.91\,\mu s$, considered in the case with $V_1 = 30\,m\,s^{-1}$. For the $V_1 = 30\,m\,s^{-1}$ calculation, the stress and plastic strain distributions at the impacted end obtained from the non-uniform mesh of Fig. 2 and from the square 20 × 40.mesh are in very good agreement.

Figures 5–9 display contours of various field quantities at four stages of crack growth for the reference case. These four stages are at $t = 41.70\,\mu s$, $t = 44.54\,\mu s$, $t = 45.11\,\mu s$ and $t = 46.25\,\mu s$. In each figure the region displayed corresponds to the deformed configuration of the region in Fig. 2b.

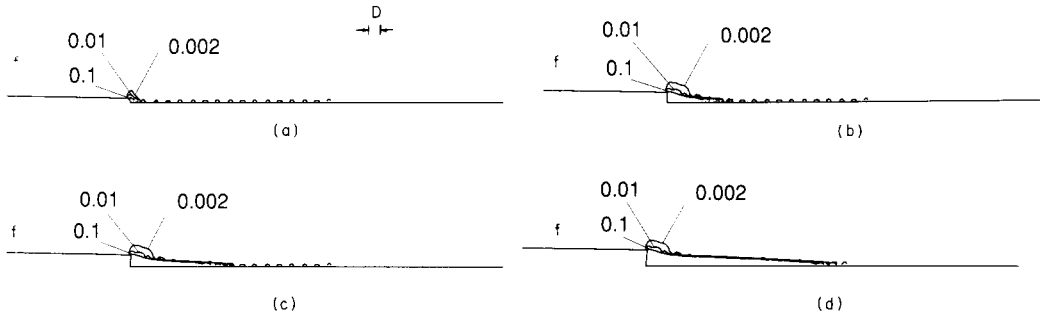

Fig. 5. Contours of constant void volume fraction, f, for the reference case. The initial particle spacing, $D = 0.1$ mm, is marked to set the scale. (a) $t = 41.70\,\mu$s (b) $t = 44.54\,\mu$s (c) $t = 45.11\,\mu$s (d) $t = 46.25\,\mu$s.

Porosity development is shown in Fig. 5. As seen in Fig. 5a, the stresses generated when the wave reaches the symmetry plane are large enough to induce void nucleation at each of the inclusions. However, the void volume fraction in the inclusions remains small (less than 1 per cent) until the advancing crack tip approaches the particle. The position of the crack surface is identified with the $f = 0.1$ contour emanating from the initial crack location, since this gives a good picture of the region within which the stress carrying capacity of the material has vanished. The amount of crack growth is denoted by Δa and defined by the

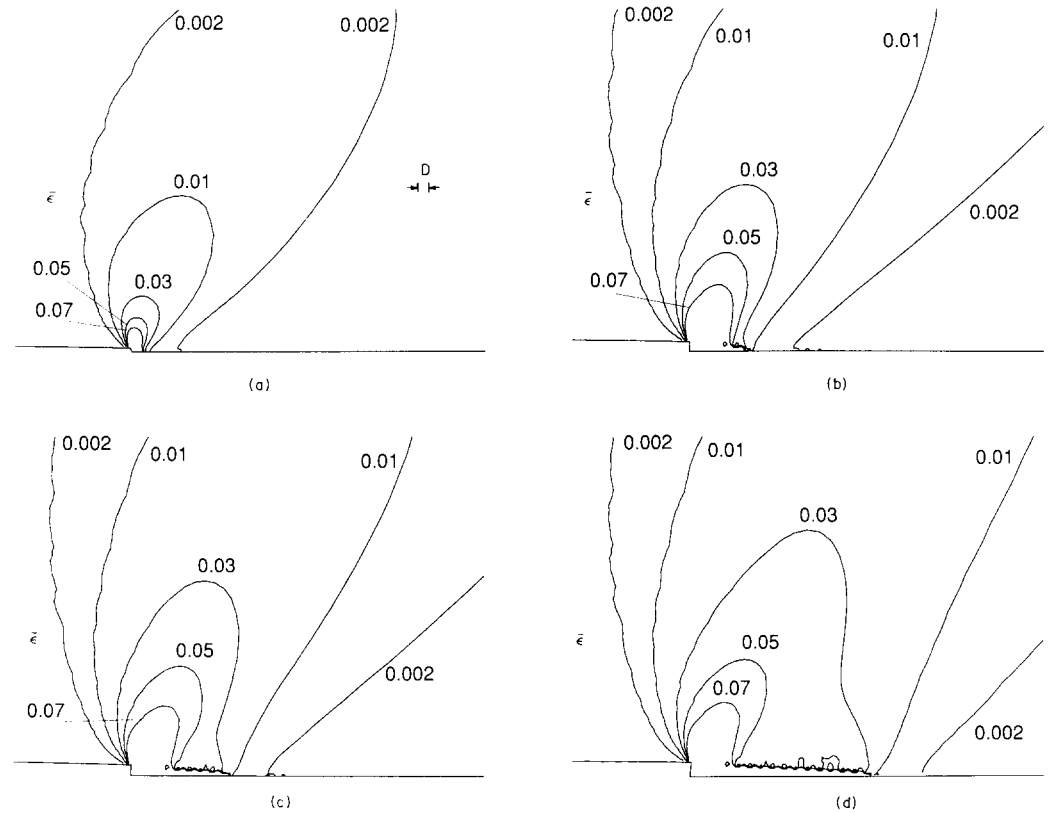

Fig. 6. Contours of constant matrix plastic strain, $\bar{\varepsilon}$, for the reference case. The initial particle spacing, $D = 0.1$ mm, is marked to set the size scale. (a) $t = 41.70\,\mu$s. (b) $t = 44.54\,\mu$s (c) $t = 45.11\,\mu$s (d) $t = 46.25\,\mu$s.

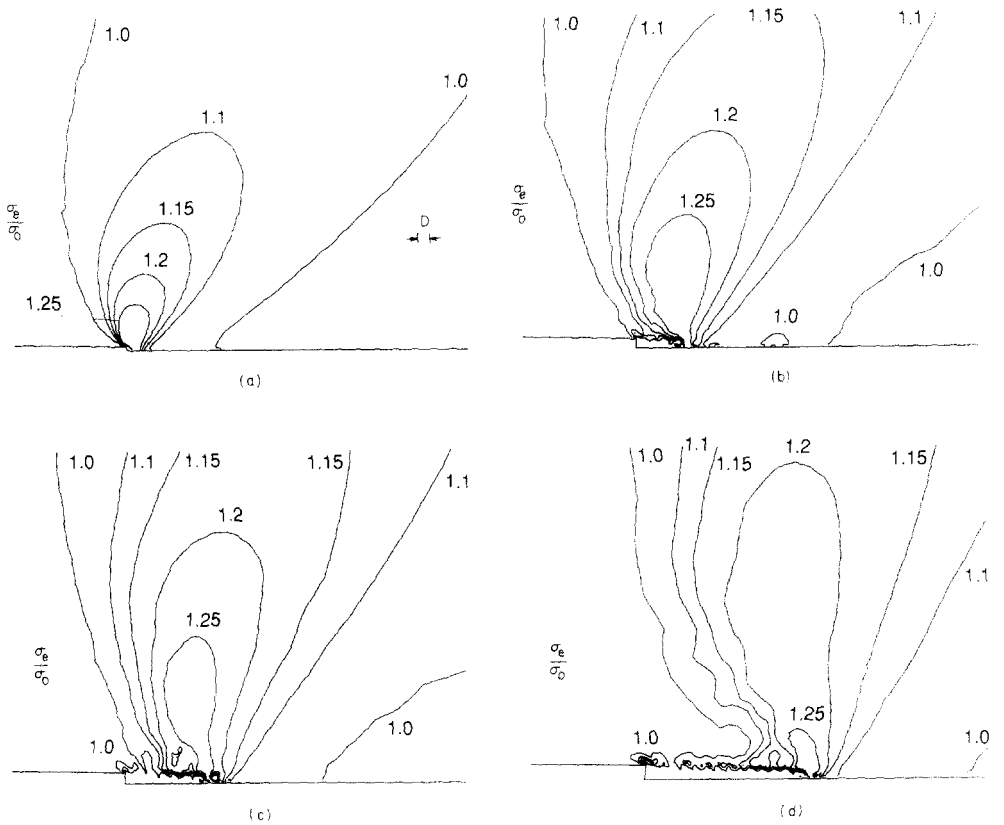

Fig. 7. Contours of constant Mises effective stress, σ_e, for the reference case. The initial particle spacing, $D = 0.1$ mm, is marked to set the size scale. (a) $t = 41.70\,\mu$s. (b) $t = 44.54\,\mu$s. (c) $t = 45.11\,\mu$s. (d) $t = 46.25\,\mu$s, $\sigma_0 = 1000$ MPa.

intersection of the $f = 0.1$ contour with $y^2 = 0$. The four stages of crack growth in Figs. 5a through 5d correspond to $\Delta a = 0.025$ mm, $\Delta a = 0.34$ mm, $\Delta a = 0.64$ mm and $\Delta a = 1.44$ mm, respectively. Note that the void volume fraction in the background Gurson material is negligible away from the fracture surface.

At $t = 41.70\,\mu$s, Fig. 5a, the crack has begun to grow but has not yet linked up with the first particle. The crack speed increases until the crack has engulfed three inclusions (in Fig. 5b the crack is between the third and fourth inclusions). Thereafter the crack speed is essentially constant at 651 m s^{-1}, which is 0.202 times the shear wave speed. The crack opening angle, defined as twice the angle between the linear portion of the $f = 0.1$ contour and the symmetry line, is nearly constant after the initial stages of growth. For the reference case shown in Fig. 5, the crack opening angle is ≈ 7 deg from Fig. 5b, $t = 45.11\,\mu$s, on. The calculation is terminated at $t = 46.25\,\mu$s, at which point the crack has grown 1.44 mm and is near the end of the uniform mesh region.

The strain concentration above the crack in Fig. 6 is expected from the HRR field, [33, 34], which gives the greatest strain concentration at about 98 deg from the crack tip for $N = 0.1$, and from previous finite deformation analyses of crack tip fields, e.g., [36, 8–10]. Crack tip blunting at the initial tip gives rise to strains of order unity. However, the strains that develop along the crack line during propagation are only moderate, becaue of the rather sharp crack profile.

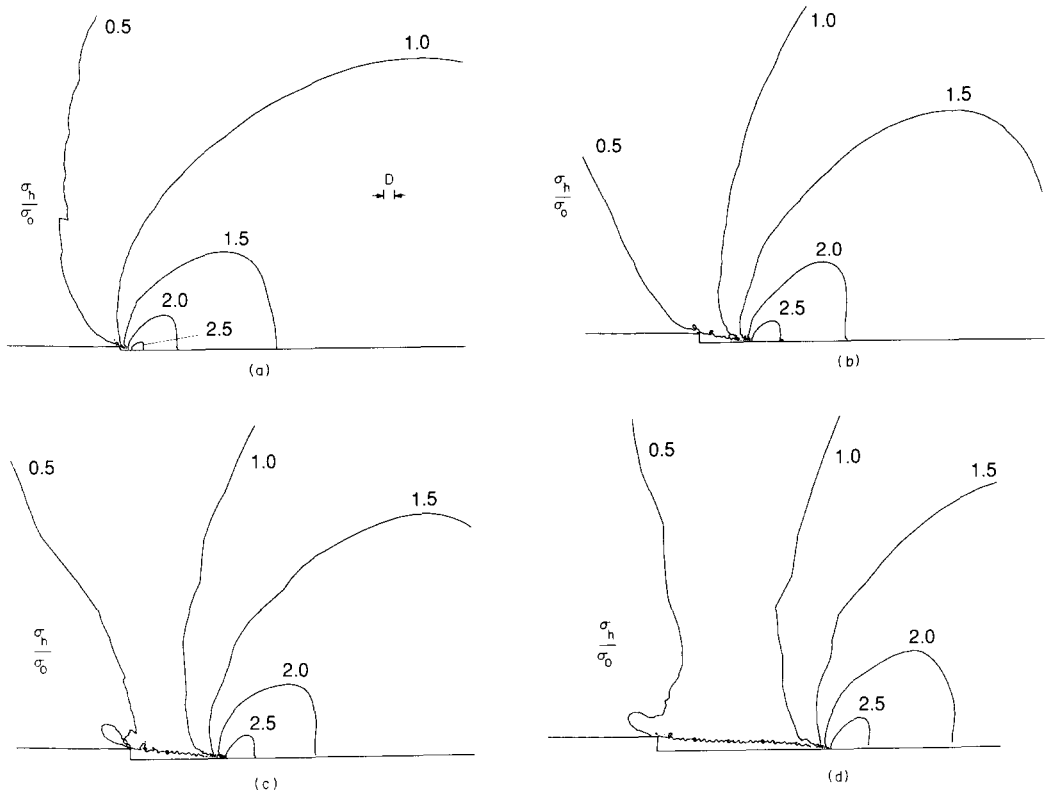

Fig. 8. Contours of constant hydrostatic tension, σ_h, for the reference case. The initial particle spacing, $D = 0.1$ mm, is marked to set the size scale. (a) $t = 41.70\,\mu$s (b) $t = 44.54\,\mu$s (c) $t = 45.11\,\mu$s (d) $t = 46.25\,\mu$s, $\sigma_0 = 1000$ MPa.

Contours of Mises effective stress, σ_e, are shown in Fig. 7. At $t = 41.70\,\mu$s the near tip effective stress contours have the form associated with a stationary crack. In Figs. 7c and 7d, the "backward leaning" of the higher valued stress contours is an effect of the higher crack speed. By way of contrast, the hydrostatic stress contours in Fig. 8 have a similar shape at all four times.

Figure 9 shows contours of constant temperature near the initiation of crack growth, at $t = 41.70\,\mu$s, and during rapid crack propagation, at $t = 46.25\,\mu$s. The large strains accompanying crack tip blunting give rise to a maximum temperature of about 320°C in the current fracture process zone in Fig. 9a, which is a 300 deg increase above the initial uniform background temperature of 20°C. The strains that occur in the process zone during propagation are smaller and so is the temperature rise. The maximum temperature near the crack tip in Fig. 9b is about 220°C.

Figures 10 and 11 show contours of various field quantities at two times for the case with $V_1 = 30\,\mathrm{m\,s^{-1}}$; in Fig. 10 $t = 42.30\,\mu$s, $\Delta a = 0.34$ mm, and in Fig. 11 $t = 43.91\,\mu$s, $\Delta a = 1.45$ mm. The main effect of the higher impact velocity is to lead to a somewhat greater speed of crack propagation than in the reference case. With $V_1 = 30\,\mathrm{m\,s^{-1}}$, the crack speed (as measured by the propagation speed of the $f = 0.1$ contour along the symmetry line) is $690\,\mathrm{m\,s^{-1}}$, which is 0.214 times the shear wave speed. As in the reference case this speed is attained after the crack has advanced about 0.4 mm and is essentially constant thereafter.

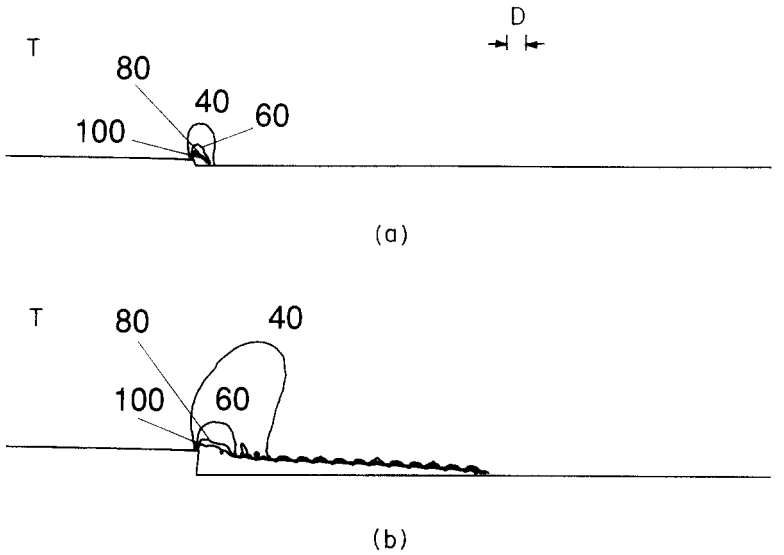

Fig. 9. Contours of constant temperature, T, for the reference case. The initial particle spacing, $D = 0.1$ mm, is marked to set the size scale. (a) $t = 41.70\,\mu$sec. (b) $t = 46.25\,\mu$s.

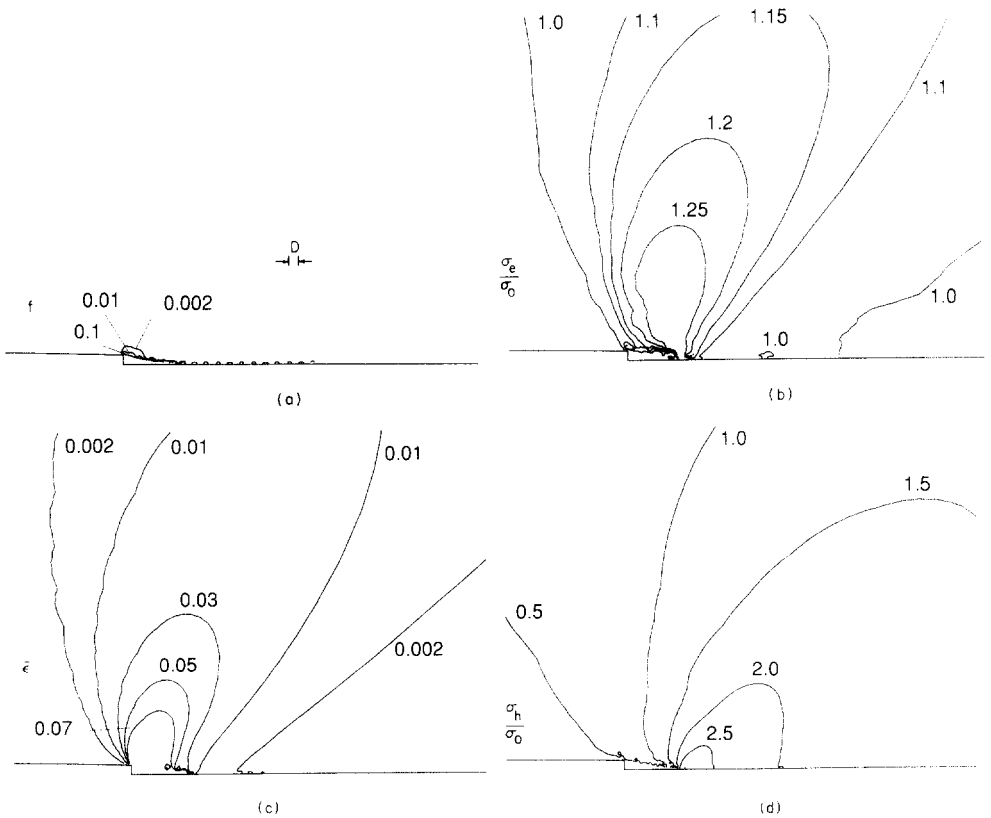

Fig. 10. Contours of various field quantities for the case with $V_1 = 30$ m/s at $t = 42.30\,\mu$s and $\Delta a = 0.34$ mm. The initial particle spacing, $D = 0.1$ mm, is marked to set the size scale. (a) Contours of constant void volume fraction f. (b) Contours of constant Mises effective stress, σ_e. (c) Contours of constant matrix plastic strain, $\bar{\varepsilon}$. (d) Contours of constant hydrostatic tension, σ_h, $\sigma_0 = 1000$ MPa.

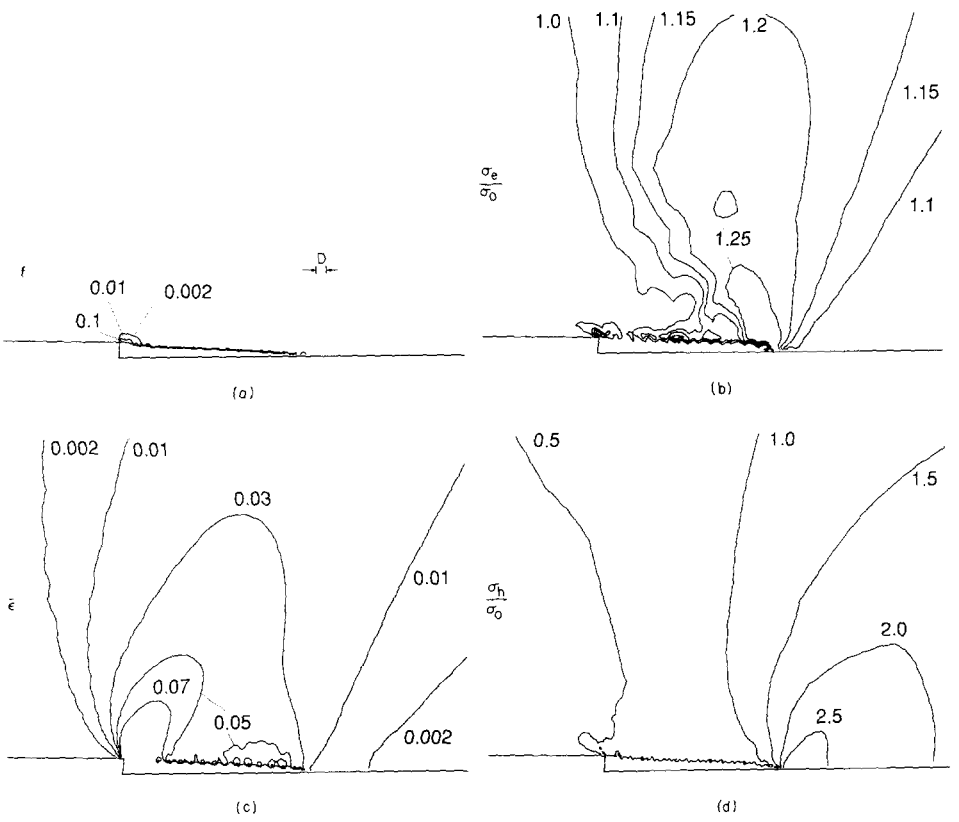

Fig. 11. Contours of various field quantities for the case with $V_1 = 30\,\mathrm{m\,s^{-1}}$ at $t = 43.91\,\mu\mathrm{s}$ and $\Delta a = 1.45\,\mathrm{mm}$. The initial particle spacing, $D = 0.1\,\mathrm{mm}$, is marked to set the size scale. (a) Contours of constant void volume fraction f. (b) Contours of constant Mises effective stress, σ_e. (c) Contours of constant matrix plastic strain, $\bar{\varepsilon}$. (d) Contours of constant hydrostatic tension, σ_h. $\sigma_0 = 1000\,\mathrm{MPa}$.

Again, as in the reference case, the crack opening angle becomes essentially constant and is also $\approx 7\,\mathrm{deg}$.

In the two cases considered in Figs. 5–11, a particular material has been subject to two loading conditions. Figures 12–14 exhibit the effect of variations in the material with the loading as in the reference case. In Fig. 12, the nucleation stress is given by $\sigma_N = 2200\,\mathrm{MPa}$ and contours of field quantities are shown at $t = 44.73\,\mu\mathrm{s}$ and $\Delta a = 1.24\,\mathrm{mm}$. Somewhat surprisingly, crack growth with $\sigma_N = 2200\,\mathrm{MPa}$ initiates earlier than for the reference case. It appears that the increased nucleation stress leads to a greater concentration of deformation at the initial crack tip which leads to an earlier initiation of crack growth. Stated another way, the more extensive early nucleation that occurs in the reference case has a crack shielding effect. The crack speed is $638\,\mathrm{m\,s^{-1}}$. As in the previous cases the crack opening angle is essentially constant after the early stages of crack growth and is $\approx 7\,\mathrm{deg}$.

Figures 13 and 14 show contours of field quantities for the case with $D = 200\,\mu\mathrm{m} = 0.2\,\mathrm{mm}$, which is twice the reference value of D, at $t = 45.11\,\mu\mathrm{s}$, $\Delta a = 0.46\,\mathrm{mm}$, and at $t = 49.66\,\mu\mathrm{s}$, $\Delta a = 1.28\,\mathrm{mm}$, respectively. Qualitatively, crack growth proceeds as in the previous cases. Quantitatively, there is a significant difference. The crack opening angle is increased to $\approx 15\,\mathrm{deg}$ and the crack speed is decreased to $182\,\mathrm{m\,s^{-1}}$. Accordingly, the strains that develop are larger than in the previous cases. It is worth noting that since the finite

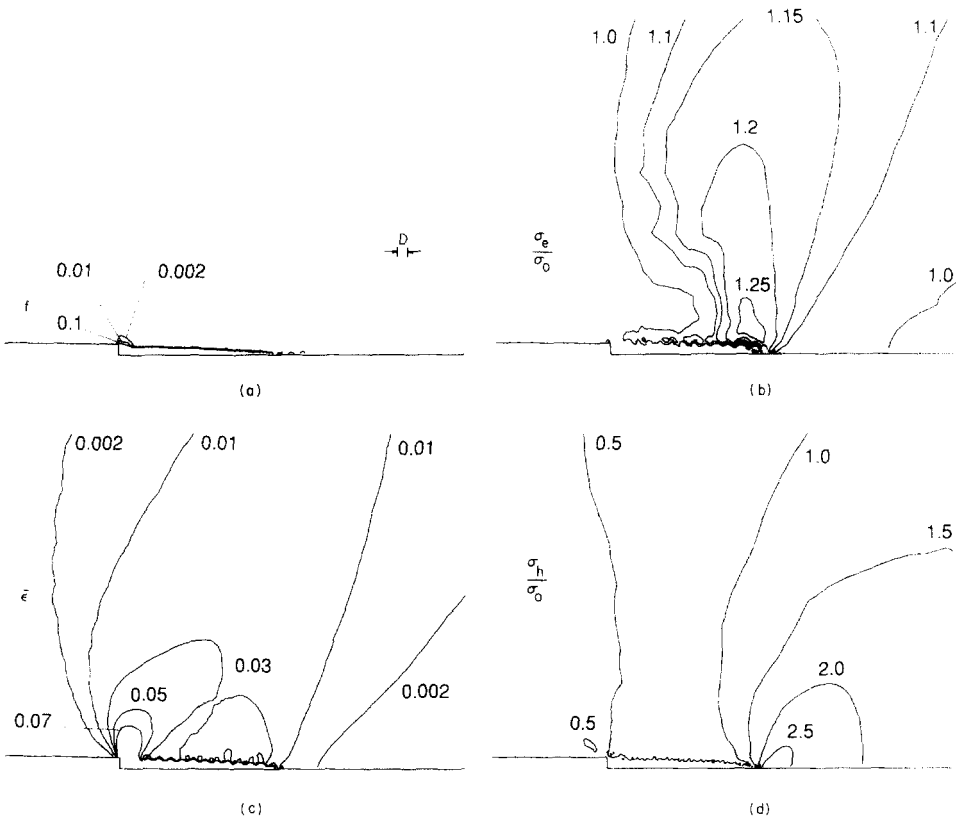

Fig. 12. Contours of various field quantities for the case with $\sigma_N = 2200\,\text{MPa}$ at $t = 44.73\,\mu\text{s}$ and $\Delta a = 1.24\,\text{mm}$. The initial particle spacing, $D = 0.1\,\text{mm}$, is marked to set the size scale. (a) Contours of constant void volume fraction f. (b) Contours of constant Mises effective stress, σ_e. (c) Contours of constant matrix plastic strain, $\bar{\varepsilon}$. (d) Contours of constant hydrostatic tension, σ_h. $\sigma_0 = 1000\,\text{MPa}$.

element mesh used in this calculation is identical to that used in the previous three calculation, the results in Figs. 13 and 14 show that neither the crack opening angle nor the crack speed are set by the mesh.

Crack growth versus time curves for the four cases analyzed are plotted in Fig. 15. The points marked in the figure correspond to times at which the crack length was measured and the curves consist of linear interpolation between these points. In each case, the crack grows at an essentially constant speed for $\Delta a \geqslant \approx 0.3\,\text{mm}$ and the crack speeds quoted previously were obtained by a least squares linear fit to the points in Fig. 15 for which $\Delta a > 0.3\,\text{mm}$, except for the case with $\sigma_N = 2200\,\text{MPa}$ where the first point used for the linear fit is $\Delta a = 0.24\,\text{mm}$. It is worth emphasizing that the development of an essentially constant crack speed in Fig. 15, as well as the crack propagating in each case with a near constant crack opening angle, are outcomes of the solution to the initial-boundary value problem posed here and are in no way imposed by the formulation.

Initially, the crack growth versus time curve is the same for each case with $V_1 = 20\,\text{m}\,\text{s}^{-1}$. It is plausible that this occurs because both the imposed loading and the background Gurson material are identical for each of these cases. The time at which constant speed growth initiates and the speed of crack propagation depend on the properties of the large inclusions. For the range of parameters considered in this investigation, the large inclusion spacing,

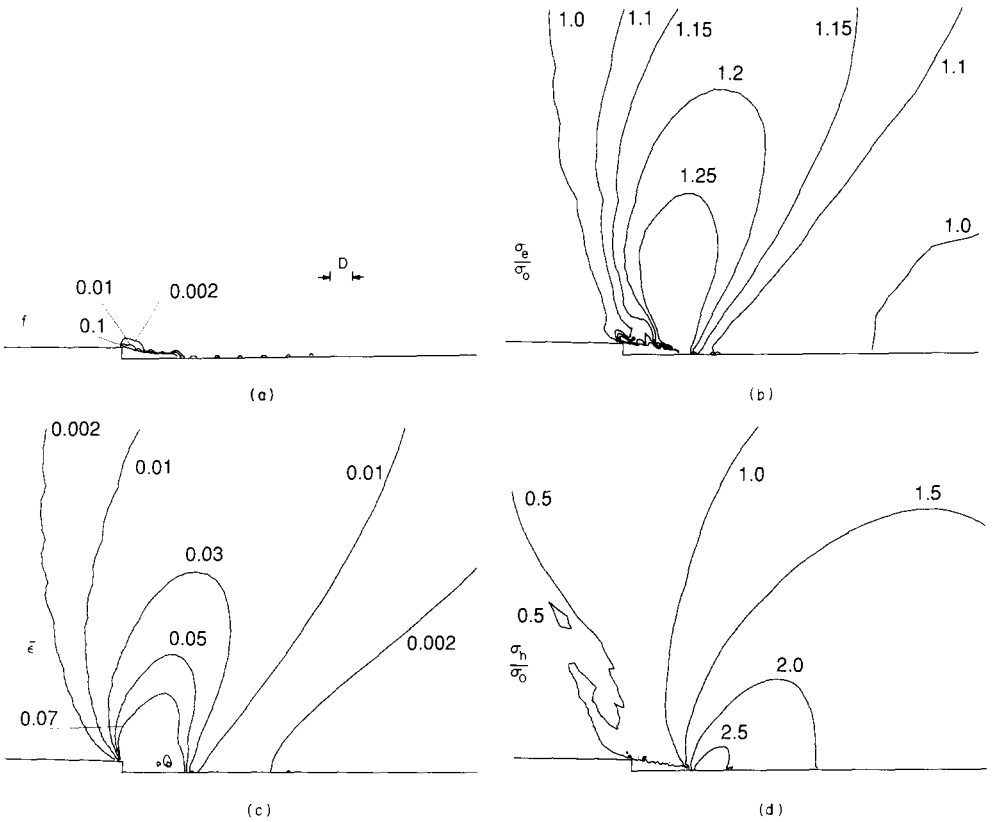

Fig. 13. Contours of various field quantities for the case with $D = 0.2\,\text{mm}$ at $t = 45.11\,\mu\text{s}$ and $\Delta a = 0.46\,\text{mm}$. The initial particle spacing, is twice the value for the reference case and is marked to set the size scale. (a) Contours of constant void volume fraction f. (b) Contours of constant Mises effective stress, σ_e. (c) Contours of constant matrix plastic strain, $\bar{\varepsilon}$. (d) Contours of constant hydrostatic tension, σ_h. $\sigma_0 = 1000\,\text{MPa}$.

D, has the greatest effect on crack speed. However, it appears clear that high enough values of the inclusion nucleation stress, σ_N, would significantly delay the onset of crack growth and slow the rate of crack propagation.

Figure 16 shows crack growth versus crack opening displacement, COD, for the reference case and the case with $V_1 = 30\,\text{m s}^{-1}$. All material properties and particle characteristics are identical for these two cases. The crack opening displacement is the opening at the initial crack tip (the point marked in Fig. 2b) and is the full COD, i.e., twice the distance between the crack flank and the symmetry line. The two curves are very close, but in Fig. 16 $\Delta a/\Delta\text{COD}$ is slightly smaller for the case with the higher imposed loading velocity and the higher crack speed.

Figure 17 shows curves of J versus time and COD versus time for the four cases. In Fig. 17a, J is given by (2.34). The contour Γ is through the ring of elements that intersect the crack line about 15 mm in front of the initial crack tip. As noted previously, the COD is the crack opening displacement at the initial crack tip. In addition to the remote value of J plotted in Fig. 17a, J was calculated on eight other contours surrounding the uniform mesh region (see Fig. 2b), progressively closer to the initial crack tip. In the early stages of crack blunting, say up to $J/(D\sigma_0) = 0.2$ for the reference case, J is essentially path independent over the outer eight contours and the area contribution in (2.34) to the remote J is of a

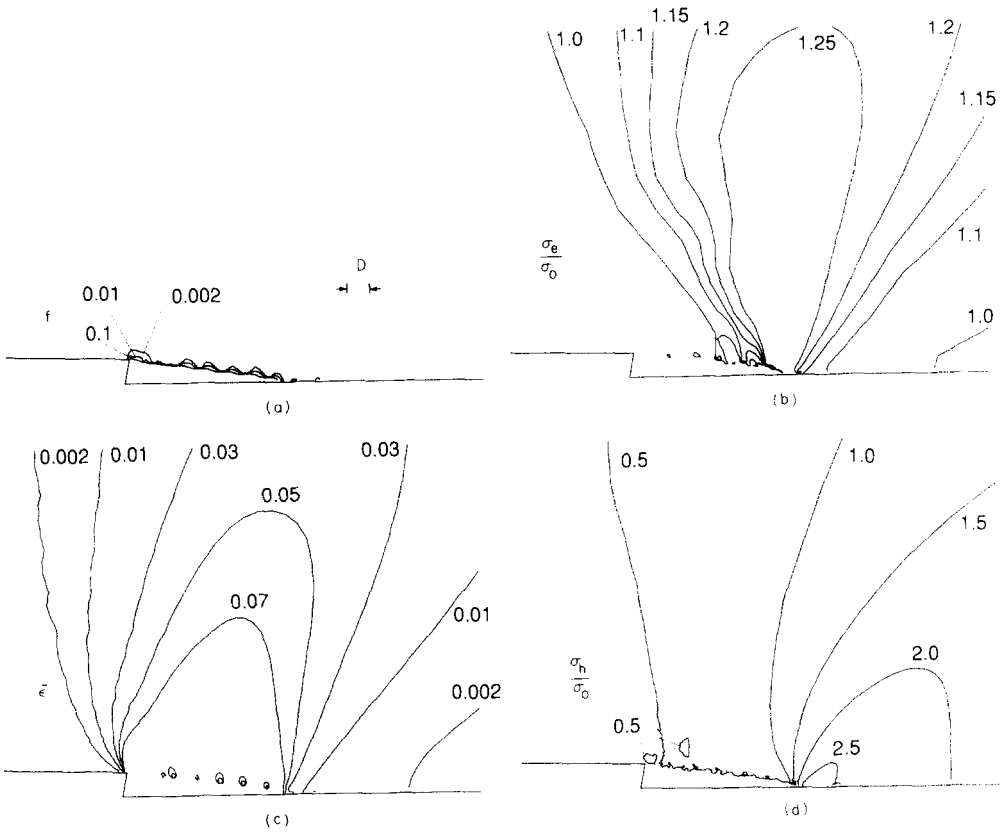

Fig. 14. Contours of various field quantities for the case with $D = 0.2\,\text{mm}$ at $t = 49.66\,\mu\text{s}$ and $\Delta a = 1.28\,\text{mm}$. The initial particle spacing, is twice the value for the reference case and is marked to set the size scale. (a) Contours of constant void volume fraction f. (b) Contours of constant Mises effective stress, σ_e. (c) Contours of constant matrix plastic strain, $\bar{\varepsilon}$. (d) Contours of constant hydrostatic tension, σ_h. $\sigma_0 = 1000\,\text{MPa}$.

comparable size to J. At later times, as plastic flow becomes more extensive, J decreases smoothly from its remote value to a value near zero at the innermost of these contours. During crack growth, the area integral in (2.34) can contribute up to 18 per cent to the value of the remote J, but with 8 to 10 per cent being a more typical contribution. The contribution of the area integral term to the value of J on the inner contours is smaller.

A value of the mode I stress intensity factor K_I can be calculated from J using the plane strain small scale yielding relation

$$K_I = \left(\frac{EJ}{1-\nu^2}\right)^{1/2}. \tag{4.1}$$

Using (4.1) for the reference case, the value $J/D\sigma_0 = 1.00$ at $t = 41.26\,\mu\text{s}$ corresponds to $K_I = 152\,\text{MPa}\sqrt{\text{m}}$, while $J/D\sigma_0 = 3.41$ at $t = 43.91\,\mu\text{s}$ corresponds to $K_I = 281\,\text{MPa}\sqrt{\text{m}}$. This gives a nominal loading rate of $\dot{K}_I = 26 \times 10^6\,\text{MPa}\sqrt{\text{m}}\,\text{s}^{-1}$. Similar calculations give nominal loading rates of $\dot{K}_I = 25 \times 10^6\,\text{MPa}\sqrt{\text{m}}\,\text{s}^{-1}$ for the case with $D = 0.2\,\text{mm}$ and $\dot{K}_I = 33 \times 10^6\,\text{MPa}\sqrt{\text{m}}/\text{s}^{-1}$ for the case with $V_1 = 30\,\text{m}\,\text{s}^{-1}$.

In Fig. 18, J from Fig. 17a is plotted against the COD from Fig. 17b. Prior to crack growth, the J versus COD curves are identical, since the plastic properties of the material

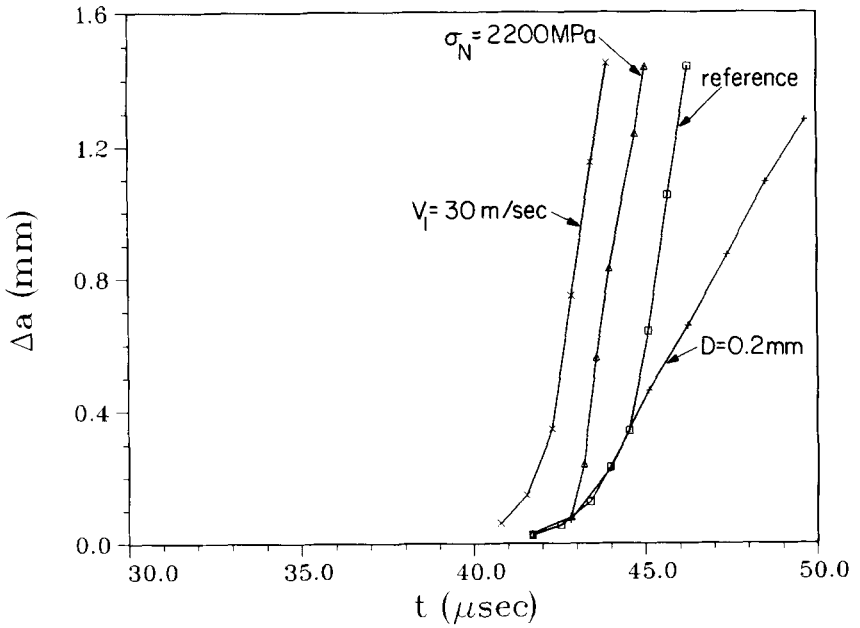

Fig. 15. Crack growth versus time. The crack length, Δa, is defined as the length of the $f = 0.1$ contour along the crack line $y^2 = 0$.

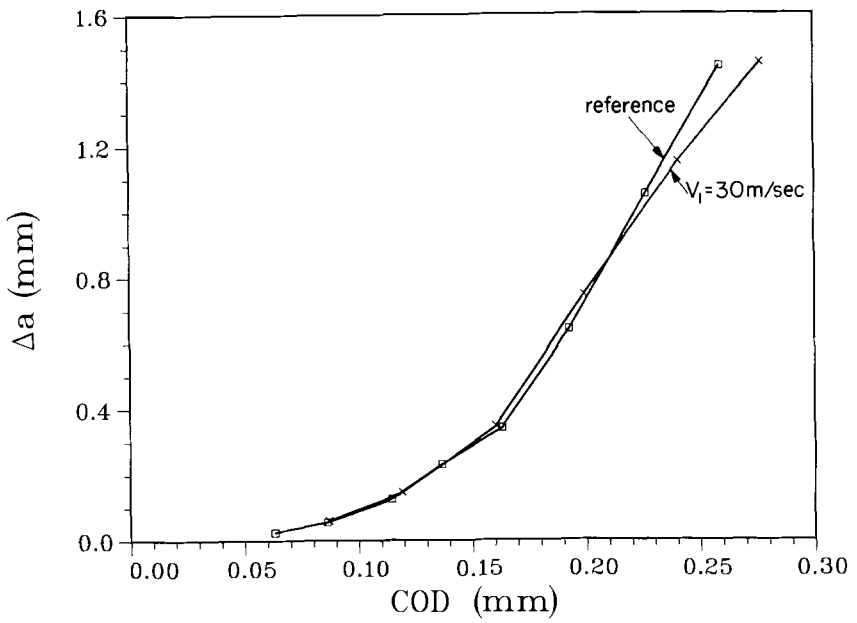

Fig. 16. Crack growth as a function of COD for the two cases where material properties and particle characteristics are identical. The COD is measured at the initial crack tip and the crack length, Δa, is defined as the length of the $f = 0.1$ contour along the crack line $y^2 = 0$.

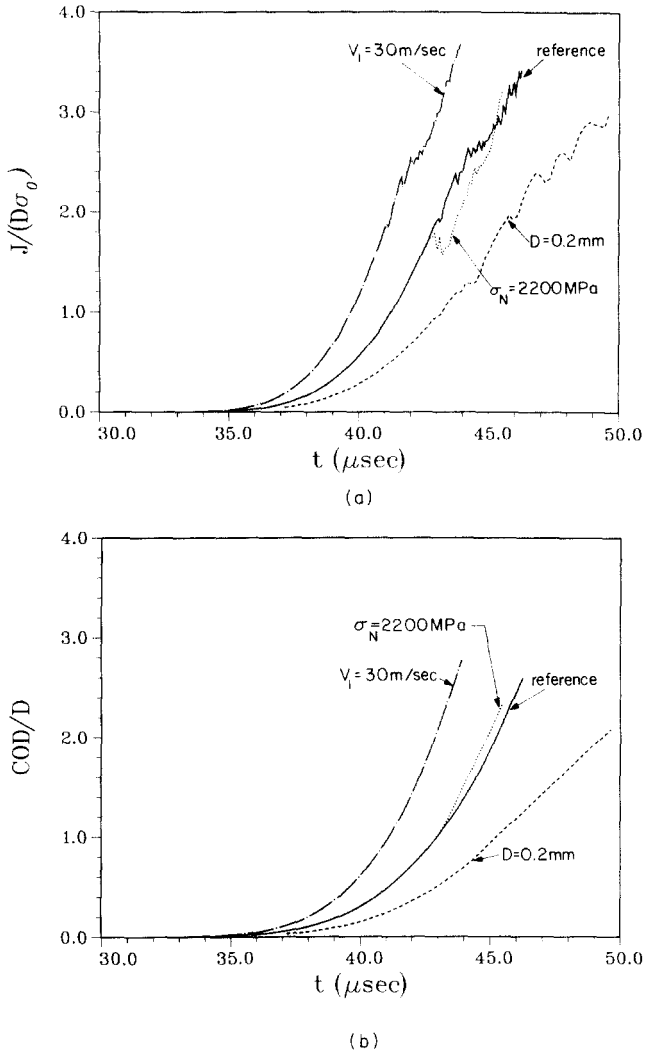

Fig. 17. (a) J versus time. J is defined by (2.34) and includes both an area integral term and a contour integral term. (b) COD versus time. The COD is measured at the initial crack tip. For three of the cases $D = 0.1$ mm. As noted on the figure $D = 0.2$ mm for the fourth case. In all cases $\sigma_0 = 1000$ MPa.

are identical for all four cases. The slope of this curve gives COD $= 0.53\, J/\sigma_0$, which is in good agreement with the COD versus J relation expected from the HRR field. For the HRR field under small scale yielding conditions and with $N = 0.1$ and $E/\sigma_0 = 250$, Shih [37] reports a slope of 0.53. The slope from the HRR field is based on small strain theory, and pertains to quasi-static deformation histories and to rate independent material response. Furthermore, (2.24) is not a pure power hardening relation and here $E/\sigma_0 = 211$. The slope in Fig. 18 is also consistent with the value ≈ 0.47 found in [10] in a quasi-static small scale yielding analysis based on a material description similar to that used here, but with $E/\sigma_0 = 500$ (with $E/\sigma_0 = 500$, the slope of the HRR small scale yielding COD-J relation is 0.50 [37]). In [10] the initial crack tip was taken to be a semi-circular notch, with a fine mesh around the notch to resolve local fields near the initial crack surface. The finite element mesh in this study has been designed to resolve extensive crack growth and does not resolve the

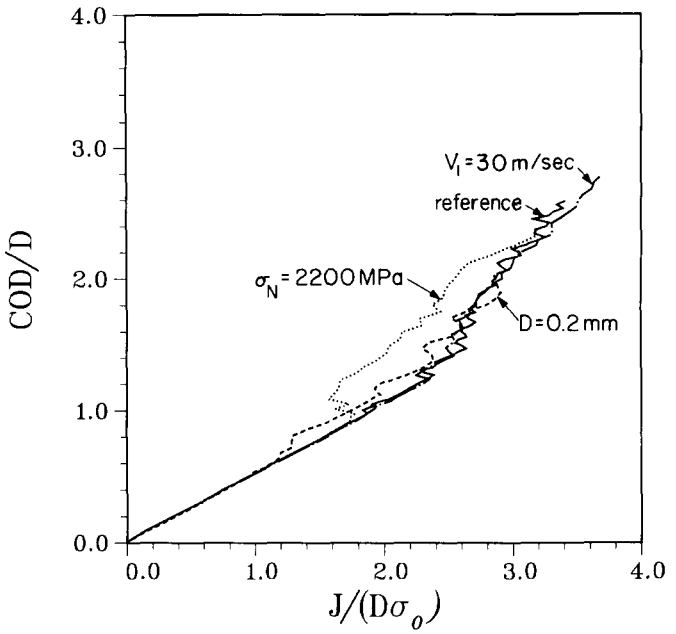

Fig. 18. J versus COD. J is defined by (2.34) and includes both an area integral term and a contour integral term. The COD is measured at the initial crack tip. For three of the cases $D = 0.1$ mm. As noted on the figure $D = 0.2$ mm for the fourth case. In all cases $\sigma_0 = 1000$ MPa.

initial blunting fields with the accuracy of the mesh in [10]. Nevertheless, the present mesh appears to give a reasonably good representation of the J versus COD relation during blunting.

There is a fairly well defined point in Fig. 18 at which the J-COD relation deviates from the blunting line (this point of deviation is less abrupt for the case with $D = 0.2$ mm than for the other three cases). This deviation occurs when failure has just begun in elements nearest the initial crack tip and occurs at about $t = 43.07\,\mu$s for the reference case, $t = 41.07\,\mu$s for the case with $V_1 = 30\,\text{m s}^{-1}$, $t = 42.72\,\mu$s for the case with $\sigma_N = 2200$ MPa and $t = 42.80\,\mu$s for the case with $D = 0.2$ mm. This is shortly before the time at which the first void links up with the initial crack tip. The times at which this initial link up occurs are about $43.2\,\mu$s for the reference case, $41.4\,\mu$s for the case with $V_1 = 30\,\text{m s}^{-1}$, $43.1\,\mu$s for the case with $\sigma_N = 2200$ MPa and $44.0\,\mu$s for the case with $D = 0.2$ mm. For reference, the loading wave first arrives at the crack line at $t = 33.2\,\mu$s. The values of J and COD at which the first void links up with the initial crack tip are: $J \approx 2.0 \times 10^5\,\text{J m}^{-2}$, COD $= 0.11$ mm for the reference case; $J \approx 2.0 \times 10^5\,\text{J cm}^{-2}$, COD $= 0.11$ mm for the case with $V_1 = 30\,\text{m s}^{-1}$; $J \approx 1.7 \times 10^5\,\text{J m}^{-2}$, COD $= 0.10$ mm for the case with $\sigma_N = 2200$ MPa and $J \approx 2.4 \times 10^5\,\text{J m}^{-2}$, COD $= 0.14$ mm for the case with $D = 0.2$ mm.

In addition to the four cases discussed so far, several other calculations were carried out. One was a calculation with all parameters at their reference value except that $V_1 = 5\,\text{m s}^{-1}$. This calculation was only continued to the linking of the first void with the initial crack tip. At this low loading rate, an unloading wave arrives at the crack tip prior to this initial link up, causing a considerable time delay. At $t = 137.6\,\mu$s, the initial void has essentially coalesced with the initial crack tip. Although there is a large time delay the value of J is about $2.0 \times 10^5\,\text{J m}^{-2}$, as in the reference case, and the corresponding COD is about 5 per cent larger than in the reference case.

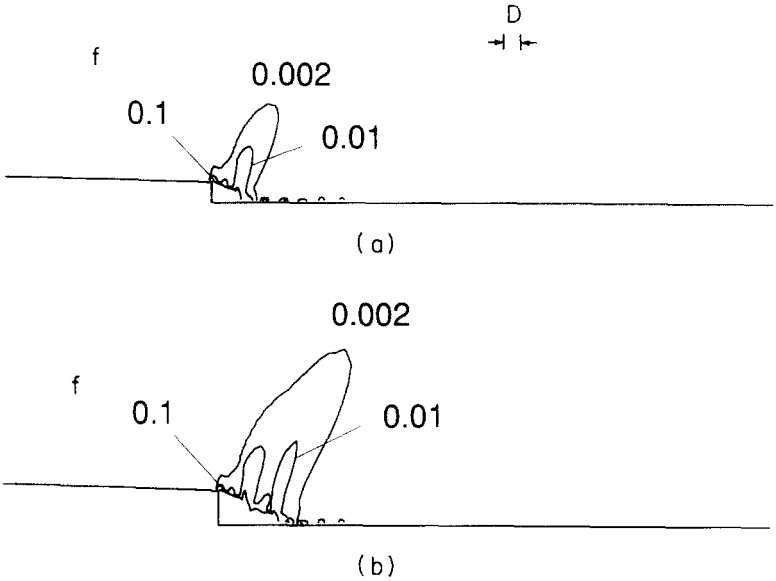

Fig. 19. Contours of constant void volume fraction for a specimen having $w = 10\,\text{mm}$, $b = 20\,\text{mm}$ and $a = 1.75\,\text{mm}$. All material properties and particle characteristics are those of the reference case. Also, the size of the elements in the uniform near-tip mesh is the same as used in the calculations for the larger specimen. The initial particle spacing, $D = 0.1\,\text{mm}$, is marked to set the size scale. (a) $t = 16.81\,\mu\text{s}$. (b) $t = 25.21\,\mu\text{s}$.

Some calculations were also carried out for a specimen proportioned as in Fig. 1, but an order of magnitude smaller, i.e., with $w = 10\,\text{mm}$, $b = 20\,\text{mm}$ and $a = 1.75\,\text{mm}$. The finite element mesh for the small specimen calculations was different from that shown in Fig. 2, but near the initial crack tip a uniform mesh was used with a $0.0208\,\text{mm} \times 0.0175\,\text{mm}$ quadrilateral element size which is nearly the same element size as in the uniform region in Fig. 2b. The small specimen undergoes general yielding and the failure behavior is quite different from that for the larger specimens. Figure 19 shows contours of constant void volume fraction at two times, $t = 16.81\,\mu\text{s}$ and $t = 25.21\,\mu\text{s}$, for a small specimen where all material properties and particle characteristics are as for the reference case. Also, the imposed loading velocity is $V_1 = 20\,\text{m}\,\text{s}^{-1}$. The region of high porosity extends further away from the fracture surface than in the large specimen calculations and the failure mode appears to be one of ductile tearing rather than one of crack growth. In addition to illustrating the dependence of failure mode on specimen size, Fig. 19 provides further confirmation that the computed failure mode is not set by the mesh.

5. Discussion

The most significant feature of the present computations is that the crack growth rates determined here are entirely based on the predictions of the micro-mechanical material model, describing ductile failure by the nucleation and growth of voids to coalescence. In previous studies of dynamic crack growth a critical value of the crack-tip-opening displacement, the dynamic stress-intensity factor, or some other parameter characterizing the near tip fields has been assumed; or the analyses have been directly based on the assumption of a constant speed of crack growth. Comparing with this type of assumption it is interesting

to note from the present results that in each case an essentially constant crack speed is predicted, after a short initial stage (Fig. 15). For the same material and specimen geometry this constant speed of crack growth is only increased by about 6 per cent when the impact velocity is increased by 50 per cent, in part, at least, due to plastic yielding at the impacted end limiting the increase in stress. When the material parameters are changed by doubling the nucleation stress for the larger particles the crack growth speed decays only slightly, by 2 per cent, whereas doubling the particle spacing gives a significant crack speed reduction by about 72 per cent. However, the crack growth speed is strongly dependent on the specimen geometry, and thus J as shown by the small specimen computation (Fig. 19), where general yielding and much lower crack speeds are found.

In the initial stage some blunting develops, associated with rather large strains and a certain amount of damage in a region around the initial crack tip. Subsequently the straining leading to crack growth by void coalescence is rather localized, and here an essentially constant crack tip opening angle is predicted in each case. This seems to support the type of crack growth criterion applied by Hoff et al. [6], where quasi-static COD versus Δa results were used for the initial part of growth, while a fixed critical value of the crack tip opening angle was used subsequently. For the reference material investigated here the critical value of this angle is about 7 deg when plastic flow is contained, but for the small specimen (Fig. 19), where general yielding occurs, the value is significantly larger, about 52 deg. Also, with contained plastic flow, it was found that doubling the particle spacing, D, led to a doubling of the crack tip opening angle.

It is noted that the very localized damage found here in the material near the surfaces of the growing crack is partly dependent on the assumption that only a single row of larger inclusions straight ahead of the crack is taken into account. As shown in Fig. 5a all these larger inclusions have started to nucleate when the wave has hit the crack plane. Therefore, if a two dimensional array of larger inclusions had been accounted for, as in [10], a two dimensional array of partially nucleated larger voids would be expected in a region around the growing crack. Then, dependent on the initial particle distribution the crack could possibly grow off the initial crack plane or zig-zag; but any concrete knowledge about that would required further investigations.

In the initial stage, where some blunting occurs, the speed of crack growth increases gradually, as shown in Fig. 15, and the initial parts of these predicted crack length versus time curves are essentially identical in the three cases where the imposed impact velocity is the same. This is significant since the prediction is entirely based on the failure criterion incorporated in the micro-mechanical material model describing ductile failure. As the larger inclusions have different nucleation stress or spacing in the three cases, it appears that the crack extension versus time relationship, during the early stages of growth, must be characteristic of the plasticity and failure criterion in the matrix material between the larger voids, for a given impact velocity and specimen geometry.

It is also interesting that the two different crack growth versus time curves corresponding to different impact velocity but identical material (Fig. 15) are nearly coincident when Δa versus COD is plotted (Fig. 16). However, this result could be expected since it has been mentioned above that the crack-tip-opening angles during dynamic crack growth are nearly the same in these two cases.

The double edge cracked rectangular bar analyzed here is assumed to be loaded symmetrically, so that equal and opposite impact velocities are prescribed at each end. It is anticipated

that this type of loading may be the result of two symmetrically placed explosive charges, which are triggered simultaneously, thus sending a symmetrical pattern of stress waves towards the cracked cross-section. It is noted that the time intervals considered in the present analyses are so short that the waves never reach the opposite end of the specimen, and therefore reflections from these ends do not play a role.

The specimen considered is somewhat similar to the circumferentially notched round bar analyzed by Nakamura, Shih and Freund [38], to model experiments of Costin, Duffy and Freund [39]. However, in these experiments the load is applied at one end of the bar and is represented in the analyses as a linearly increasing applied load. One consequence of this loading arrangement is that the full specimen has to be modelled numerically; but another significant difference is that the loading in [38, 39] gives rise to a single stress wave coming from one end of the bar, whereas the two symmetric stress waves considered in the present analyses hit the cracks simultaneously. The superposition of these two stress waves gives rise to extra high stress levels in the crack tip regions, and therefore the present results for symmetric loading would not be directly comparable with results for the same specimen loaded only at one end.

Since high strain rates occur in the crack tip region during dynamic crack growth it is expected that material strain rate sensitivity plays an important role. Such rate sensitivity is incorporated in the present analyses through the elastic-viscoplastic material model. One particular value of the rate hardening exponent, representative of structural steels, has been used here, but the increased strain rate sensitivity that appears to come into play at strain rates of $\approx 10^6$, Klopp et al. [40], is not accounted for. A detailed quantitative understanding of the effect of rate sensitivity could be obtained by a more extensive parameter study, using the present computational procedure.

Adiabatic heating due to plastic dissipation is unavoidable at rapid crack growth in ductile materials. Here two effects of heating are accounted for, thermal softening viscoplastic behavior and thermal expansion. The computations show a maximum temperature increase of about 300°C in the fracture process zone (Fig. 9), which is clearly enough to have a noticeable effect on the local stress fields. However, a computation for the small specimen in which temperature changes were neglected indicated that these thermal effects do not greatly affect the crack growth behavior in the cases considered, because porosity has the dominant softening effect.

Acknowledgements

The support of the Office of Naval Research through contract N00014-86-K-0262 and grant N00014-89-J-3054 is gratefully acknowledged. The computations reported on here were carried out on the Cray YMP at the Pittsburgh Supercomputer Center and on a Stellar Computer GS1000 workstation. We thank Professor M. Giles of the Department of Aeronautics and Astronautics at MIT who kindly provided graphics software used in the analysis and presentation of these results.

References

1. K.B. Broberg, in *Recent Progress in Applied Mechanics*, K.B. Broberg, J. Hult and F. Niordson (eds.), Wiley, New York (1967) 125–151.

2. L.B. Freund, *Journal of the Mechanics and Physics of Solids* 20 (1972) 129–140.
3. B. Brickstad and F. Nilsson, *International Journal of Fracture* 16 (1980) 71–84.
4. J.F. Kalthoff, *International Journal of Fracture* 27 (1985) 277–298.
5. J. Ahmad, J. Jung, C.R. Barnes and M.F. Kanninen, *Engineering Fracture Mechanics* 17 (1983) 235–246.
6. R. Hoff, C.A. Rubin and G.T. Hahn, *Engineering Fracture Mechanics* 26 (1987) 445–461.
7. L.B. Freund and Y.J. Lee, *International Journal of Fracture* 42 (1990) 261–276.
8. S. Aoki, K. Kishimoto, A. Takeya and M. Sakata, *International Journal of Fracture* 28 (1984) 267–278.
9. N. Aravas and R.M. McMeeking, *International Journal of Fracture* 29 (1985) 21–38.
10. A. Needleman and V. Tvergaard, *Journal of the Mechanics and Physics of Solids* 35 (1987) 151–183.
11. R. Becker, A. Needleman, S. Suresh, V. Tvergaard, and A.K. Vasudevan, *Acta Metallurgica* 37 (1989) 99–120.
12. V. Tvergaard and A. Needleman, *Journal of the Mechanics and Physics of Solids* 34 (1986) 213–241.
13. V. Tvergaard and A. Needleman, *International Journal of Fracture* 37 (1988) 197–215.
14. A.L. Gurson, *Plastic Flow and Fracture Behavior of Ductile Materials Incorporating Void Nucleation, Growth and Interaction*, Ph.D thesis, Brown University (1975).
15. A.L. Gurson, *Journal of Engineering Materials and Technology* 99 (1977) 2–15.
16. J. Pan, M. Saje and A. Needleman, *International Journal of Fracture* 21 (1983) 261–278.
17. V. Tvergaard, *International Journal of Fracture* 17 (1981) 389–407.
18. V. Tvergaard, *International Journal of Fracture* 18 (1982) 237–252.
19. V. Tvergaard and A. Needleman, *Acta Metallurgica* 32 (1984) 157–169.
20. C.C. Chu and A. Needleman, *Journal of Engineering Materials and Technology* 102 (1980) 249–256.
21. G.I. Taylor and H. Quinney, *Proceedings of the Royal Society of London* A143 (1934) 307–326.
22. T. Nakamura, C.F. Shih and L.B. Freund, *International Journal of Fracture* 27 (1985) 229–243.
23. C.F. Shih, B. Moran and T. Nakamura, *International Journal of Fracture* 30 (1986) 79–102.
24. B. Moran and C.F. Shih, *Engineering Fracture Mechanics* 27 (1987) 615–642.
25. B. Moran and C.F. Shih, *International Journal of Fracture* 35 (1987) 295–310.
26. T. Belytschko, R.L. Chiapetta and H.D. Bartel, *International Journal for Numerical Methods in Engineering* 10 (1976) 579–596.
27. R.D. Krieg and S.W. Key, *International Journal for Numerical Methods in Engineering* 7 (1973) 273–286.
28. D. Peirce, C.F. Shih and A. Needleman, *Computers and Structures* 18 (1984) 875–887.
29. V. Tvergaard, *Journal of the Mechanics and Physics of Solids* 30 (1982) 399–425.
30. J.R. Rice, *Journal of Applied Mechanics* 35 (1968) 379–386.
31. J. Koplik and A. Needleman, *International Journal of Solids and Structures* 24 (1988) 835–853.
32. R. Becker, A. Needleman, O. Richmond and V. Tvergaard, *Journal of the Mechanics and Physics of Solids* 36 (1988) 317–351.
33. J.W. Hutchinson, *Journal of the Mechanics and Physics of Solids* 16 (1968) 13–31.
34. J.R. Rice and G.F. Rosengren, *Journal of the Mechanics and Physics of Solids* 16 (1968) 1–12.
35. K. Cho, J.P. Skelnak and J. Duffy, in *Fracture Mechanics: Twenty-First Symposium*, ASTM STP 1074, (J.P. Gudas, J.A. Joyce and E.M. Hackett (eds.)), American Society for Testing and Materials, Philadelphia, in press.
36. R.M. McMeeking, *Journal of the Mechanics and Physics of Solids* 25 (1977) 357–381.
37. C.F. Shih, *Journal of the Mechanics and Physics of Solids* 29 (1981) 305–326.
38. T. Nakamura, C.F. Shih and L.B. Freund, *Engineering Fracture Mechanics* 22 (1985) 437–452.
39. L.S. Costin, J. Duffy and L.B. Freund, in *Fast Fracture and Crack Arrest*, ASTM STP 627, G.T. Hahn and M.F. Kanninen (eds.)), American Society for Testing and Materials, Philadelphia (1977) 301–318.
40. R.W. Klopp, R.J. Clifton and T.G. Shawki, *Mechanics of Materials* 4 (1985) 375–385.